ELSEVIER

Physics of the Earth and Planetary Interiors 124 (2001) 193–211

PHYSICS OF THE EARTH AND PLANETARY INTERIORS

www.elsevier.com/locate/pepi

# The relative density-to-shear velocity scaling in the uppermost mantle

Frédéric Deschamps*, Roel Snieder[1], Jeannot Trampert

*Department of Geophysics, Utrecht University, Budapestlaan 4, P.O. Box 80021, 3508 TA Utrecht, The Netherlands*

Received 25 October 2000; received in revised form 12 March 2001; accepted 15 March 2001

**Abstract**

We perform inversions of gravity data (geopotential model EGM96) and seismic tomography model (S16RLBM) for the scaling factor ($\zeta$), which relates relative density anomalies to relative S-wave velocity anomalies. The gravity data and tomographic model are anti-correlated below continents down to a depth of $z = 200$ km. This anti-correlation is not present below oceans. Except for smoothness, which is controlled by a damping factor, no a priori information is added to the inversion. Data are filtered between degrees $\ell = 11$ and $\ell = 16$ of the spherical harmonic expansion. This spectral window is well suited for the study of intermediate-size (2000–4000 km) anomalies in the uppermost mantle. Calculations are made separately for sub-continental and sub-oceanic mantle. The sub-continental and sub-oceanic scaling factors are significantly different at depths shallower than 260 km. In both cases, the magnitude of $\zeta$ is around 0.05. The sub-continental scaling factor has a positive root down to $z = 220$ km, whereas the sub-oceanic scaling factor yields positive values down to $z = 140$ km only. At depth shallower than 350 km, models of $\zeta$ do not depend on the damping factor or the viscosity model. At depths greater than 350 km, the resolution of $\zeta(z)$ decreases significantly and low degrees ($\ell = 2$–4) add information from large-scale anomalies and from the lower mantle. As a result, the shape and values of $\zeta$ for $\ell = 2$–16 and $\ell = 11$–16 are significantly different at depths greater than 350 km. A possible explanation of the discrepancies between the sub-continental and sub-oceanic scaling factor is that intermediate-scale anomalies are more important in the continental uppermost mantle than in the oceanic uppermost mantle. 

*Keywords:* S-wave velocity anomalies; Density anomalies; Mantle structure

## 1. Introduction

The density ($\rho$) and the S-wave velocity ($V_S$) of the Earth's mantle are both related to temperature, composition and pressure. Therefore, the inference of the density structure from $V_S$-anomalies is not straightforward. To make a crude diagnostic of the origin of the anomalies, one can use a scaling factor ($\zeta$) defined as the ratio of the relative density variations to the relative $V_S$-anomalies.

$$\zeta(r,\theta,\varphi) = \frac{\partial \ln \rho(r,\theta,\varphi)}{\partial \ln V_S(r,\theta,\varphi)} \tag{1}$$

Purely thermal anomalies result in positive values of $\zeta$, because an increase (decrease) of temperature lowers (raises) both the density and the shear velocity. Extrapolations of experimental data for olivine yield values of $\zeta$ between 0.35 and 0.45, depending on temperature (Isaac et al., 1989; Isaac, 1992). Karato (1993) accounted for anelasticity and found

* Corresponding author.
*E-mail address:* deschamp@geo.uu.nl (F. Deschamps).
[1] Present address: Department of Geophysics, Colorado School of Mines, Golden, CO 80401, USA.

0031-9201/01/$ – see front matter 
PII: S0031-9201(01)00199-6

smaller values: $0.2 \leq \zeta \leq 0.3$ in the upper mantle. Vacher et al. (1996) have computed values of $\zeta$ using a simplified mineralogical model of the upper mantle and temperature distributions predicted by isoviscous convection. They found values of $\zeta$ ranging between 0.42 at the surface, and 0.37 at $z = 660$ km depth. To determine $\zeta$ in the mantle, one needs two independent data sets, which constrain seismic velocity and density, respectively. Here, we used a global S-wave velocity model and geodetic data.

Seismic tomography of the upper mantle yields high-velocity roots below continents, but not below oceans (for recent S-wave models see Woodhouse and Trampert, 1995; Li and Romanowicz, 1996; Su and Dziewonski, 1997; Ritsema et al., 1999). This difference was first pointed out by Jordan (1975), who proposed that material in the sub-continental mantle is colder than in the sub-oceanic mantle. The increase of density induced by the relatively low temperature is balanced by differences in the respective chemical composition of the sub-continental and sub-oceanic mantle. Forte et al. (1994a) computed a radial model of $\zeta$ related to the continent–ocean anomalies of seismic velocities, and arrived at similar conclusions.

Inversions of gravity data and tomographic models have been performed (e.g. King and Masters, 1992; Kogan and McNutt, 1993; Forte et al., 1994a,b) to investigate chemical differences in the mantle. These studies are based on flow models driven by density anomalies, and they use Eq. (1) to convert velocity anomalies into density anomalies. However, King and Masters (1992) and Kogan and McNutt (1993) have assumed a constant value of $\zeta$ throughout the mantle. Forte et al. (1994a,b) have imposed the shape of the function $\zeta(r)$, and inverted gravity data for the parameters describing this curve. Moreover, the spatial resolution of these studies is limited to the spherical harmonic degrees less or equal to $\ell = 8$ (Forte et al., 1994a,b) or $\ell = 12$ (Kogan and McNutt, 1993). Low degrees of the gravity anomalies depend strongly on the structure of the deep mantle, and are weakly influenced by medium-size ($L \sim 2000$–$4000$ km) anomalies in uppermost mantle ($z < 400$ km).

In the present study, we invert $V_S$-anomalies and gravity anomalies for a radial model of $\zeta$ without assuming a priori values or shape. We have used the global S-wave model S16RLBM (Woodhouse and Trampert, 1995), which is expressed in a spherical harmonic expansion up to degree and order 16, and the geoid model EGM96 (Lemoine et al., 1998). Calculations are made separately for oceanic and continental regions. It turns out that $\zeta$ has positive values down to $z = 220$ km below continents, and down to $z = 140$ km below oceans. At depths greater than 350 km, $\zeta$ is not well constrained. A variety of tests suggest that these results are robust.

## 2. Method and data

Inversions presented in this paper are carried out using a relationship between the gravity anomalies ($\delta g$), the $V_S$-anomalies ($\delta V_S$) and the scaling factor ($\zeta$). For each degree $\ell$ of the spherical harmonic expansion, the gravity anomaly ($\delta g_\ell$) is related to the integrated density anomaly ($\delta \rho_\ell$) weighted by the geoid kernels ($G_\ell$) (e.g. Forte and Peltier, 1987).

$$\delta g_\ell(\theta, \varphi) = \frac{3 g_0}{\bar{\rho} R} \frac{\ell - 1}{2\ell + 1} \int_{r_{\mathrm{CMB}}}^{R} G_\ell(r) \delta \rho_\ell(r, \theta, \varphi)\, \mathrm{d}r \quad (2)$$

where $R$ and $\bar{\rho}$ are the Earth's radius and mean density, $r_{\mathrm{CMB}}$ the radius of the core, and $g_0$ the acceleration of gravity at the surface.

The geoid kernels ($G_\ell$) describe the geoid response to a given density anomaly located at a given depth, and they depend on mantle dynamics. In the present study, we have computed these kernels following the method proposed by Forte and Peltier (1991). The conservation of mass, momentum, and the stress–strain relationship are expanded in terms of generalized spherical harmonics and solved for the poloidal flow in a compressible mantle. This method accounts for radial viscosity variations, and therefore it is possible to test different dynamical models of the Earth's mantle. However, the effects due to the toroidal flow, which imply lateral viscosity variations, are not considered here. Fig. 1 represents geoid kernels for the viscosity profile MF2 developed by Mitrovica and Forte (1997). For degrees up to $\ell = 8$ (Fig. 1b), the geoid kernels have non-negligible values throughout the mantle. On the other hand, at higher degrees ($\ell > 10$) (Fig. 1c), the geoid kernels yield small values in the deep ($z > 1000$ km) mantle. Therefore, the lowest degrees of the gravity anomalies integrate density anomalies over the whole mantle, whereas degrees higher than

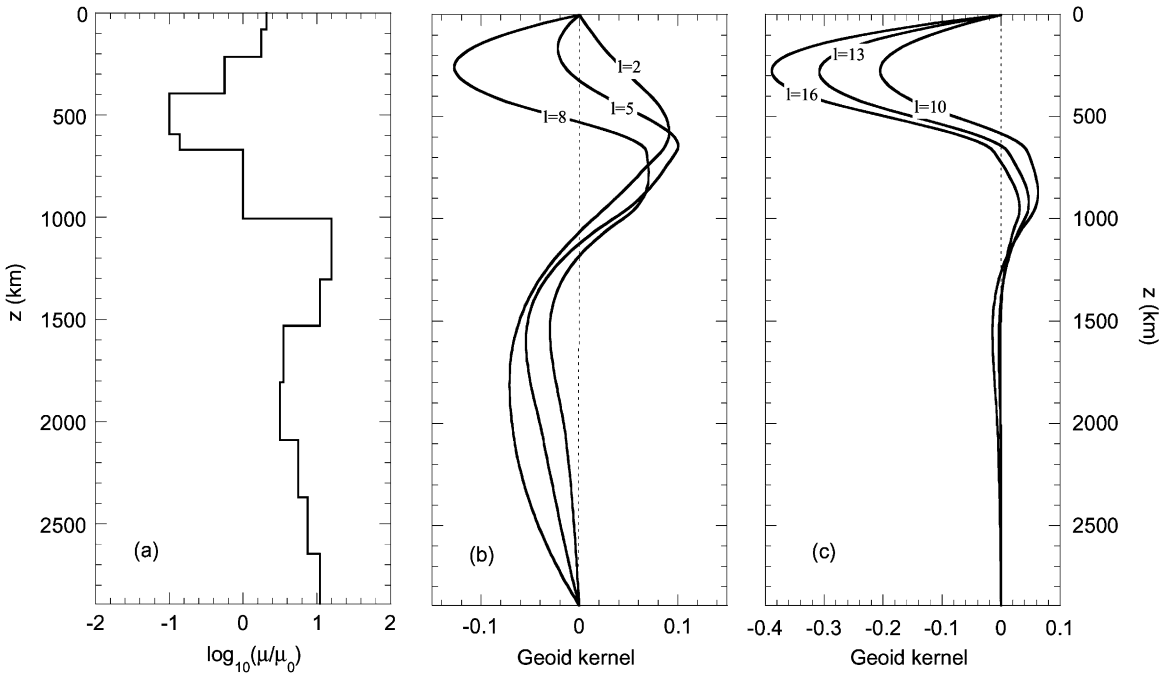


Fig. 1. Geoid kernels computed for the viscosity model MF2 (Mitrovica and Forte, 1997), and for degrees 2, 5 and 8 (left) and 10, 13 and 16 (right) of the spherical harmonic expansion. The computational method is fully described in Forte and Peltier (1991).

$\ell = 10$ are mostly sensitive to density anomalies in the upper mantle ($z < 700$ km). Similar conclusions can be drawn for other viscosity models, although the shape of the kernel changes. For a constant viscosity, kernels have negligible values in the deep mantle ($z > 1000$ km) only for degrees higher than $\ell = 20$.

Inserting Eq. (1) into Eq. (2), one can relate the density variations to the $V_S$-anomalies. If one assumes that the scaling factor does not vary laterally within a given region, Eq. (2) becomes

$$\delta g_\ell(\theta,\varphi) = \frac{3g_0}{\bar{\rho}R}\frac{\ell-1}{2\ell+1}\int_{r_{CMB}}^{R} G_\ell(r)\rho_0(r)\zeta(r) \times \frac{(\delta V_S)_\ell(r,\theta,\varphi)}{V_0(r)}\,dr \quad (3)$$

where $\rho_0(r)$ and $V_0(r)$ are the reference profiles for density and S-wave velocity, respectively. Note that one could have used geoid heights ($\delta N$) rather than gravity anomalies, since

$$\delta N_\ell(\theta,\varphi) = \frac{1}{\ell-1}\frac{R}{g_0}\,\delta g_\ell(\theta,\varphi) \quad (4)$$

The geoid is dominated by degrees $\ell = 2$ and $\ell = 3$. The root-mean-square (rms) amplitude of the geoid decreases sharply as the spherical harmonic degree increases: for $\ell = 10$ and $\ell = 20$, the rms amplitude is, respectively, 6.8 and 1.8% of that for $\ell = 2$. In comparison, the spectrum of the rms amplitude of gravity anomalies is much flatter: for $\ell = 10$ and $\ell = 20$, the rms amplitude is, respectively, 61.5 and 34.6% of that for $\ell = 2$. As a consequence, to sample structures smaller than ~4000 km, gravity anomalies carry more information than geoid heights.

Gravity and $V_S$-anomalies are then summed up for spherical harmonic degrees between $\ell_1$ and $\ell_2$.

$$\delta g(\theta,\varphi) = \sum_{\ell=\ell_1}^{\ell_2}\delta g_\ell(\theta,\varphi) \quad (5)$$

$$K(r,\theta,\varphi) = \frac{3\rho_0(r)g_0}{\bar{\rho}R}\sum_{\ell=\ell_1}^{\ell_2}\frac{\ell-1}{2\ell+1}\,G_\ell(r) \times \frac{(\delta V_S)_\ell(r,\theta,\varphi)}{V_0(r)} \quad (6)$$

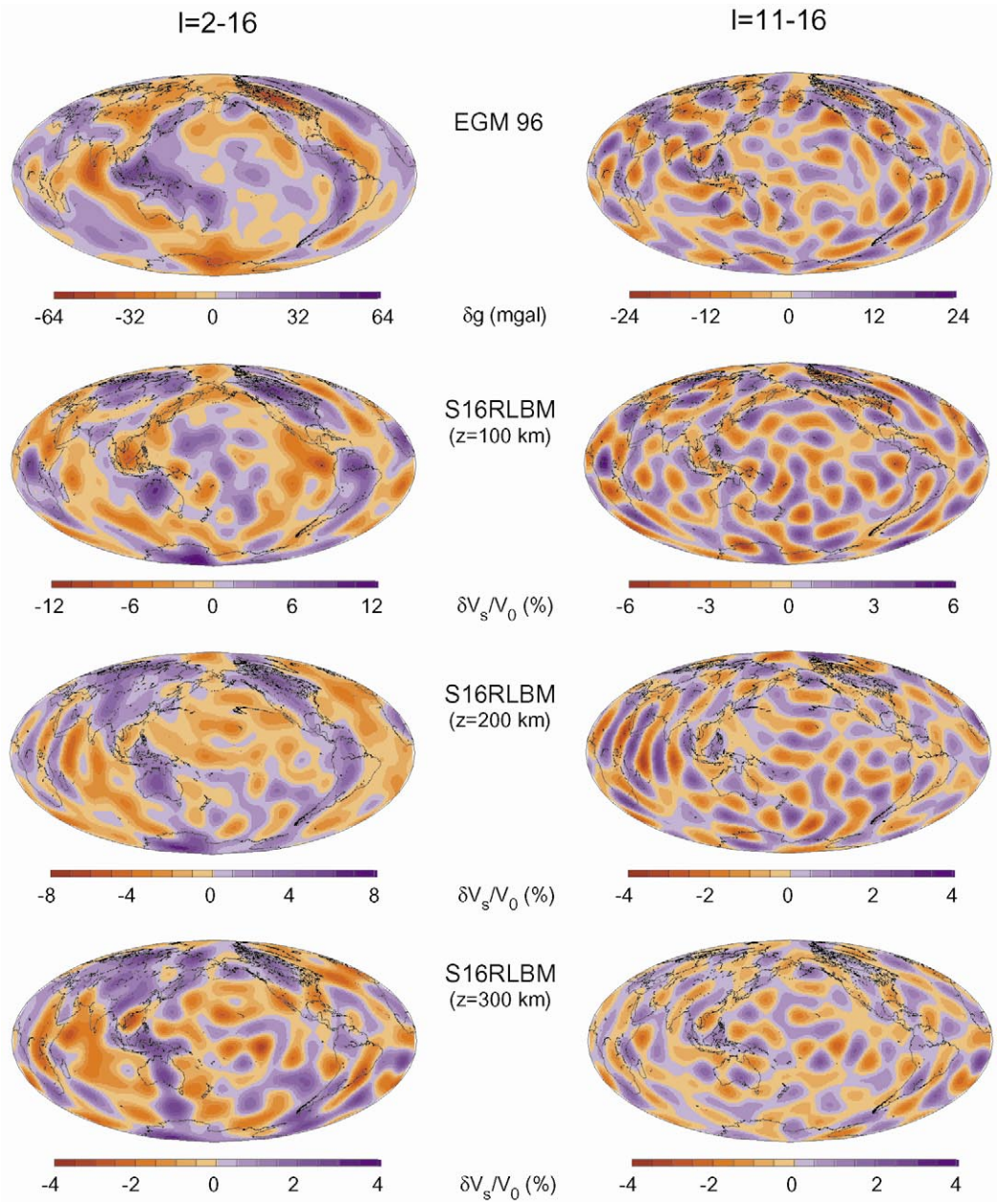


Fig. 2. Gravity anomalies from EGM96 (Lemoine et al., 1998) (top row) and S-wave velocity anomalies S16RLBM (Woodhouse and Trampert, 1995) at $z = 100$, 200 and 300 km depth. Models are filtered for degrees $\ell = 2$–16 (left column) and $\ell = 11$–16 (right column) of the spherical harmonics expansion.

Eq. (3) becomes

$$\delta g(\theta, \varphi) = \int_{r_{\mathrm{CMB}}}^{R} K(r, \theta, \varphi)\zeta(r)\,\mathrm{d}r \tag{7}$$

We have solved Eq. (7) for a radial model of scaling factor using a generalized inversion method (e.g. Snieder and Trampert, 1999). This method is outlined in Appendix A. Gravity anomalies constitute the data vector, while $V_S$-anomalies and geoid kernels are used to define the generalized inverse matrix. The inversion is regularized using a smoothness constraint with a damping factor $\varepsilon$. No other a priori information is introduced.

In the following calculations gravity anomalies and $V_S$-anomalies are sampled with an interval of $\mathrm{d}\theta$ in colatitude and $\mathrm{d}\varphi$ in longitude. To avoid over-sampling at high latitudes, the longitude interval ($\mathrm{d}\varphi$) increases from the equator to the poles, such that the surface element ($\mathrm{d}\Omega = \sin\theta \times \mathrm{d}\theta \times \mathrm{d}\varphi$) is constant. For instance, if $\mathrm{d}\varphi = 5^\circ$ on the equator, then $\mathrm{d}\Omega = 7.6 \times 10^{-3}$ steradian and $\mathrm{d}\varphi = 28.8^\circ$ at $\theta = 20^\circ$.

Inversions can be made for a selected geographical area. Here, we have computed radial models of $\zeta$ for oceans and continents separately. To define oceanic areas and continental areas, we have constructed a continent–ocean function derived from the 3SMAC tectonic regionalization (Nataf and Ricard, 1996). This data set has a resolution of $2^\circ \times 2^\circ$. The zero-mean continent–ocean function computed with the 3SMAC repartition is equal to 0.631 for continental areas and $-0.369$ for oceanic areas. The spherical harmonic expansion of this continent–ocean function is dominated by degrees 4 and 5. Hence, the continental and oceanic contributions to degrees 11 to 16 of gravity data and tomographic models are distinct.

The gravity data ($\delta g$) are tide-free, non-hydrostatic free-air gravity anomalies derived from the model EGM96 (Haagmans et al., 1998; Lemoine et al., 1998). EGM96 represents the Earth's gravitational potential up to spherical harmonic degree $\ell = 360$, and includes recent satellite tracking data and terrestrial gravity data. To remove the hydrostatic rotational flattening, we used the model of Nakiboglu (1982). The $V_S$-anomalies ($\delta V_S$) are provided by the global tomographic model S16RLBM (Woodhouse and Trampert, 1995), and the reference models of density ($\rho_0(r)$) and velocity ($V_0(r)$) are given by PREM (Dziewonski and Anderson, 1981). In S16RLBM, the three-dimensional $V_S$-anomalies structure is obtained from the inversion of Love and Rayleigh phases velocities (Trampert and Woodhouse, 1995) together with body waveform data. The model is expanded laterally in spherical harmonics up to degree $\ell = 16$ and vertically on a spline basis, leading to a vertical resolution of about 75 km in the top 400 km of the mantle. Fig. 2 shows EGM96 and S16RLBM at different depths for $\ell = 2$–16 and $\ell = 11$–16.

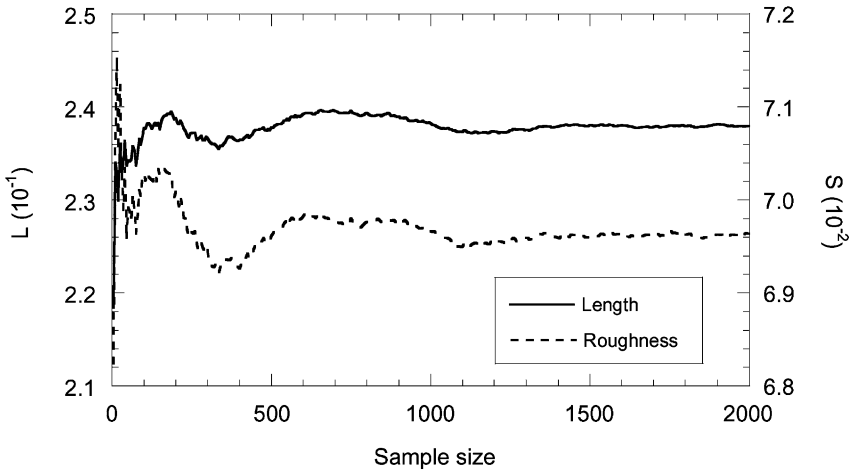


Fig. 3. Length ($\bar{L}$) and roughness ($\bar{S}$) of the mean model, as a function of the sample size. To reach stable values of $\bar{L}$ and $\bar{S}$, one must consider a large enough collection of perturbated models. This example corresponds to the sub-continental scaling factor represented in Fig. 6a.

The model S16RLBM does not provide error estimates on the $V_S$-anomalies. These errors would propagate to the values of $\zeta$. To account for likely uncertainties, we have introduced a priori errors in the original tomographic model, which leads to an estimate of the variance in $\zeta(\sigma_\zeta)$. We have generated random errors with a Gaussian probability distribution (e.g. Press et al., 1989, pp. 191–203) and added them to the local values of the relative $V_S$-anomalies ($\delta V_S/V_0$). The distribution of these errors has a zero mean and a variance $\sigma_{\text{err}}$. In other words, 95% of the simulated errors have values within $\pm 2\sigma_{\text{err}}$. We thus obtain an ensemble of perturbed tomographic models, and invert each of these models for a perturbed radial model of the scaling factor ($\zeta_{\text{per}}$). Finally, at each depth, we compute the mean value ($\bar{\zeta}$) and the variance ($\sigma_\zeta$) over the collection of the estimated models $\zeta_{\text{per}}$. To get statistically relevant values of the scaling factor, one must consider a large enough collection of perturbed models (sample size). A good test is provided by the length ($\bar{L}$) and the roughness (i.e. the norm of the derivative, $\bar{S}$) of the mean model (Appendix A). A satisfactory solution is reached when the values of $\bar{L}$ and $\bar{S}$ are independent of the sample size (Fig. 3).

## 3. Correlation between gravity and $V_S$-anomalies

At shallow depths, S16RLBM correlates with surface tectonics and yields strong continent–ocean differences down to $z = 250$ km depth (Woodhouse and Trampert, 1995). In the sub-continental mantle, between 60 and 180 km depth, S16RLBM is strongly anti-correlated with surface heat flow (Röhm et al., 2000). Röhm et al. (2000) used the depth consistency of S16RLBM to define a seismic lithosphere in the sub-continental mantle: the correlation of the $V_S$-anomalies with respect to the $V_S$-anomalies at a reference depth of 100 km falls off rapidly below 180 km. Here, we computed the correlation ($C$) between S16RLBM and the gravity anomalies derived from EGM96.

$$C(z) = \frac{1}{\sigma_{\delta g}\sigma_{\delta V_S}(z)\Omega}\int_\Omega \delta V_S(z,\theta,\varphi)\delta g(\theta,\varphi)\,\mathrm{d}\Omega \quad (8)$$

where the correlation is computed over the spatial domain $\Omega$, $\sigma_{\delta V_S}(z)$ is the variance in the $V_S$-anomalies at depth $z = R - r$ and $\sigma_{\delta g}$ the variance in the gravity anomalies.

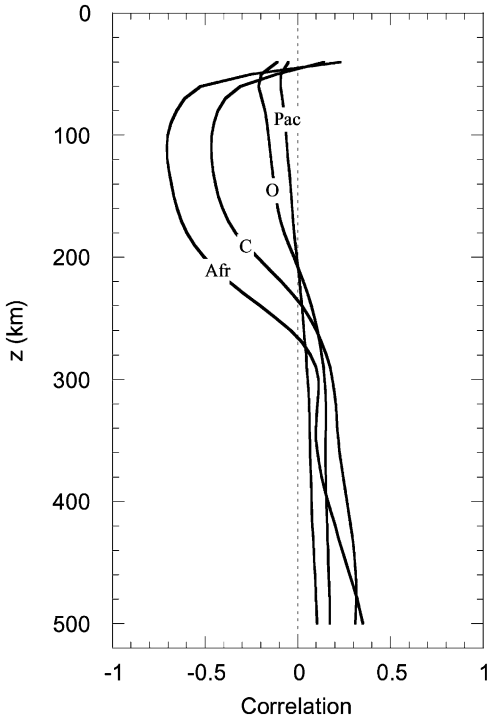


Fig. 4. Coefficient of correlation between S16RLBM $V_S$-anomalies and EGMG96 gravity anomalies as a function of depth, and for different regions. Data are filtered for the degrees $\ell = 11$–16 of the spherical harmonic expansion. C: all continental regions, O: all oceanic regions, Afr: Africa and Pac: Pacific. The resolution $\mathrm{d}\theta \times \mathrm{d}\varphi$ of the calculation is $2^\circ \times 2^\circ$ for regional areas, and $5^\circ \times 5^\circ$ for continents and oceans.

Fig. 4 shows the correlation as a function of depth for some regions. In the shallow sub-continental mantle, S16RLBM and EGM96 are anti-correlated (i.e. high $\delta V_S$ correspond to low $\delta g$). For instance, the sub-African mantle yields a root between the depths $z = 70$ and $z = 180$ km, in which the value of $C$ lies between $-0.6$ and $-0.7$ (Fig. 4). A similar root is observed in the whole-sub-continental mantle, although the anti-correlation is weaker (around $-0.5$). On the other hand, in the sub-oceanic mantle, we do not find a significant correlation between gravity and $V_S$-anomalies. In the sub-Pacific mantle, the correlation is between $-0.1$ and 0.1 at least down to $z = 500$ km. Higher correlation is seen in the shallow sub-Atlantic mantle (not shown in Fig. 4), but

in the whole sub-oceanic mantle, correlation remains small, between −0.2 and 0.2. We have also computed correlation between $V_S$-anomalies and geoid anomalies, and found results similar to those in Fig. 4.

The root observed in the sub-continental mantle is very similar in shape to that reported by Röhm et al. (2000). Thus, the seismic lithosphere is associated with negative gravity anomalies. Moreover, S-wave velocity profiles yield strong positive anomalies in the sub-continental mantle (Woodhouse and Trampert, 1995; Röhm et al., 2000). The strong anti-correlation between tomographic models and geodetic data suggests that the positive $V_S$-anomalies in the sub-continental mantle may be related to an excess of mass (positive density anomalies). However, it does not provide information about the origin of such an excess of mass. The pronounced anti-correlation between the surface heat flux and the tomographic model S16RLBM (Röhm et al., 2000) favors a thermal origin, but one cannot exclude compositional origin and other effects. For instance, accounting for anelasticity may reduce the amplitude of temperature anomalies associated with velocity anomalies (Karato, 1993).

## 4. Scaling factor in the uppermost mantle

### 4.1. Preferred model

We performed a series of 2000 inversions including simulated errors in the relative $V_S$-anomalies. This sample size is big enough to provide relevant values of the mean scaling factor (Fig. 3). We assumed a variance of the distribution of the errors ($\sigma_{err}$) equal to 2% for continental areas and 1% for oceanic areas. For $\ell = 2$–16, the mean value of the relative $V_S$-anomalies below continents (oceans) in the uppermost mantle varies between $\overline{\delta V_S/V_0} \sim 2\%$ (−1%) and $\overline{\delta V_S/V_0} \sim 0.5\%$ (−0.5%). For $\ell = 11$–16, these mean relative anomalies are about one order of magnitude smaller (solid curves in Fig. 6). Therefore, taking $\sigma_{err} = 2\%$ for continents and $\sigma_{err} = 1\%$ for oceans will simulate errors as large as 100% of the original tomographic model for $\ell = 2$–16, and even more if one considers $\ell = 11$–16. Such large simulated errors should cover most sources of possible real errors.

Geoid kernels were computed according to the viscosity model MF2 (Mitrovica and Forte, 1997), which results from joint inversion of gravity anomalies and relative sea level variations. For degrees higher than $\ell = 11$, the geoid kernels peak around $z = 250$ km depth (Fig. 1c), and have small values in the lower mantle. The lowest degrees ($\ell = 2$–8), on the other hand, have non-negligible values throughout the mantle. Moreover, for degrees lower than $\ell = 11$ the horizontal wavelength of the anomalies is larger than 4000 km. To get a good sampling of the shallow mantle ($z = 50$–400 km), we removed low degrees of gravity and $V_S$-anomalies. Here, data are summed up for the spherical harmonic degrees $\ell = 11$–16. Since geoid kernels for $\ell = 11$–16 have low values in the lower mantle, Eq. (7) is integrated from a depth of 1000 km up to the surface.

The damping factor ($\varepsilon$) controls the relative importance of a priori information (here, the smoothness) and data. To choose its value, we have performed a set of experiments in which the original (i.e. non-perturbed) $V_S$-anomalies are inverted for $\zeta(z)$ as a function of $\varepsilon$. The results are displayed on a trade-off curve (Fig. 5), by plotting the misfit of the reconstructed to observed gravity anomalies as a function of roughness of the estimated model. Usually, one defines the preferred model as the best compromise between the smoothness and the variance reduction. The trade-off curves in Fig. 5 have a hyperbolic shape, and therefore the preferred model is located on the respective elbow of these curves. According to this criterion, the variance reduction of the preferred continental model is equal to 30%, which corresponds to a damping factor around 400. The correlation between the observed and reconstructed gravity anomalies reaches 56%. For oceans, the variance reduction and the correlation are poorer (10 and 31%, respectively), and the preferred value of the damping is around 250. We did similar experiments for other spatial resolutions, and noted that for a given value of the variance reduction, $\varepsilon$ is roughly multiplied by 2 as the spatial resolution is divided by 2.

The mean value ($\bar{\zeta}$) and the variance ($\sigma_\zeta$) of the estimated model are shown in Fig. 6 for continents (left) and oceans (right). The sub-continental scaling factor (Fig. 6a) is positive down to $z = 220$ km, and has a local maximum around $z = 120$ km. It reaches a minimum at $z = 500$ km, and remains negative down to $z = 600$ km. However, the variance of the model increases with depth. The resolution matrix (Fig. 7)

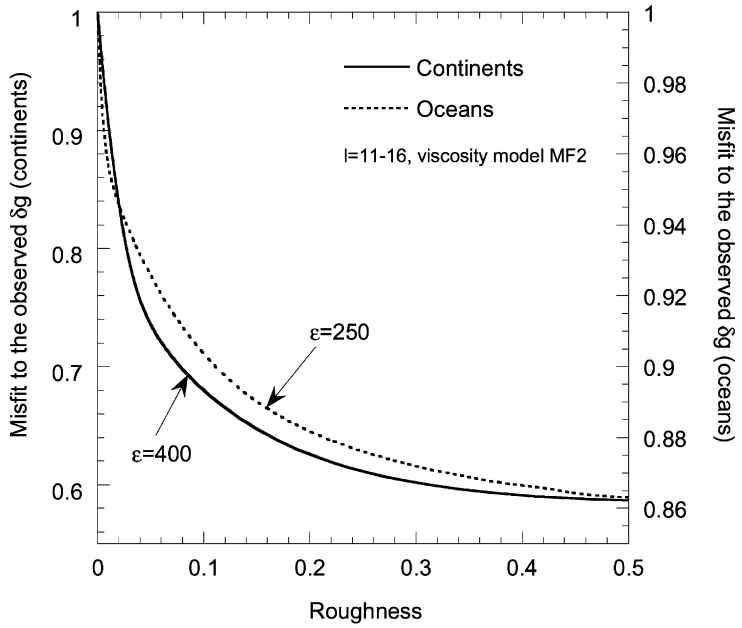


Fig. 5. Trade-off curve for the choice of the damping factor ($\varepsilon$), for continents (plain curve) and oceans (dashed curve). Inversions of gravity anomalies and original $V_S$-anomalies are carried out with different values of $\varepsilon$. The misfit to the observed gravity anomalies ($1-X$) is plotted as a function of the model roughness ($S$). Rough models yield a good variance reduction, whereas very smooth models have a poor variance reduction. A relevant value of $\varepsilon$ should lie on the elbow of the curve in between these two end-members, as indicated by the arrows. Data were filtered out in the range $\ell = 11$–16, and the surface element was kept constant, with $d\theta = 5^\circ$ and $d\varphi = 5^\circ$ on the equator.

yields substantial smearing between 300 and 450 km depth. At depths greater than 450 km, the scaling factor is poorly resolved. This poor resolution has two origins. First, the geoid kernels for $\ell = 11$–16 peak in the layer $z = 100$–400 km, and have small values in the deeper mantle. In particular, the geoid kernels are close to zero around $z = 650$ km, and the resolution is poor around this depth. Second, the amplitude of the S16RLBM anomalies decreases rapidly at depths greater than about 400 km (Woodhouse and Trampert, 1995). Therefore, any interpretation concerning the transition zone ($z = 420$–670 km) and the lower mantle is difficult. We have also reconstructed gravity data from $\bar{\zeta}$ and the original $V_S$-anomalies. The variance reduction of this synthetic data set to the observed gravity anomalies is equal to 29.3%, which is close to the variance reduction obtained by inverting the original $V_S$-anomalies. The sub-oceanic scaling factor (Fig. 6b) decreases down to $z = 180$ km and is positive down to $z = 140$ km. In the layer $220 \leq z \leq 280$ km, it remains close to zero. The variance reduction to the observed gravity data is equal to 8.9%, which is significantly poorer than for continental areas. At depths greater than 260 km, the sub-continental and sub-oceanic scaling factors are close to each other.

One may note that the variance reduction of the observed to reconstructed gravity anomalies is quite poor. First, it must be noted that the damping imposes a low variance reduction. Second, most of the gravity signal is in low degrees. For $\ell = 11$–16 gravity anomalies have small absolute values, and therefore small absolute errors can lead to high relative errors. Moreover, the variance reduction compares reconstructed gravity anomalies to observed gravity anomalies, but it does not account for errors on the observed gravity anomalies ($\sigma_{\delta g}$), on the tomographic model ($\sigma_{\delta V_S}$), and on the inverted model of $\zeta$ ($\sigma_\zeta$). To account for these errors, we performed a $\chi^2$-test. For the whole Earth, and assuming $\sigma_{\delta g} = 0.15$ mgal, $\sigma_{\delta V_S}/\delta V_S = 10\%$ and the $\sigma_\zeta$ plotted in Fig. 6a, we find $\chi^2 = 4.3$. Therefore, the gravity anomalies predicted by our inverted model of scaling factor yield within $\pm 2\sigma_{\delta g}$ of the observed gravity anomalies. Note that because the correlation

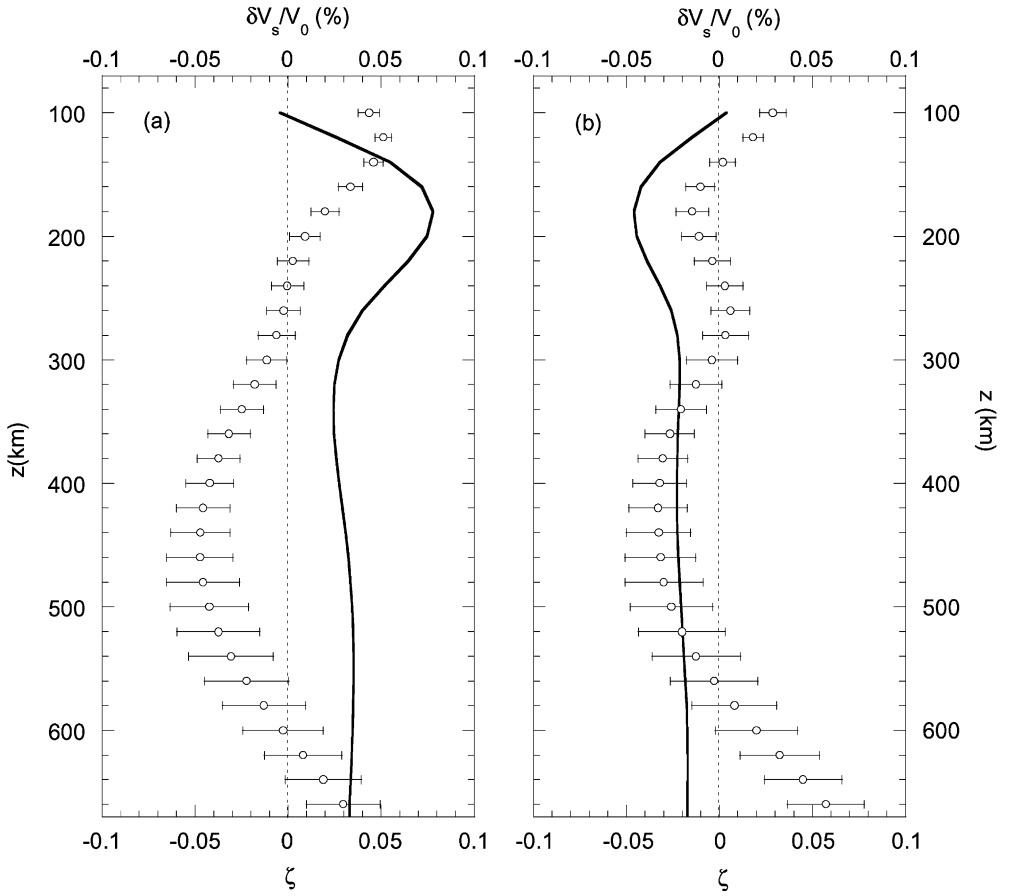


Fig. 6. Inverted scaling factor ($\zeta$) in the sub-continental (a) and sub-oceanic (b) upper mantle. Open circles indicate the mean value of $\zeta$, and the error bars represent the variance in $\zeta$. The damping factor is equal to 400 and 250 for continents and oceans, respectively. Data are filtered for degrees $\ell = 11$–16, integration (7) is performed from $z = 1000$ km depth up to the surface, and the viscosity model is MF2. The bold curve represents the mean relative $V_S$-anomalies for degrees $\ell = 11$–16 as a function of depth below continents (a) and oceans (b). Note that these mean relative anomalies are roughly one order of magnitude smaller that of the total tomographic model.

between observed and reconstructed gravity anomalies is only about 50%, our model of $\zeta(z)$ cannot explain the observed gravity anomalies completely.

The bold plain curves in Fig. 6 represent the mean value of relative $V_S$-anomalies (for degrees $\ell = 11$–16) as a function of depth, in the sub-continental (left) and sub-oceanic (right) mantle. Clearly, these curves have very different shapes than those of the scaling factor. Therefore, the results of joint inversions do not yield simply the variations of $V_S$-anomalies with depth. Chemical, thermal and/or physical processes may be responsible for the change in the sign of $\zeta$ in the uppermost mantle, as well as for the difference between the sub-continental and sub-oceanic scaling factor.

Results in Fig. 6 were obtained for given values of some input parameters that may be unsuitable for the uppermost mantle. Therefore, to test the robustness of these results, it is important to evaluate the influence of parameters such as the smoothness and the radial viscosity model.

### 4.2. Damping factor ($\varepsilon$)

To evaluate the influence of a priori information on the estimated model of $\zeta$, we performed other series

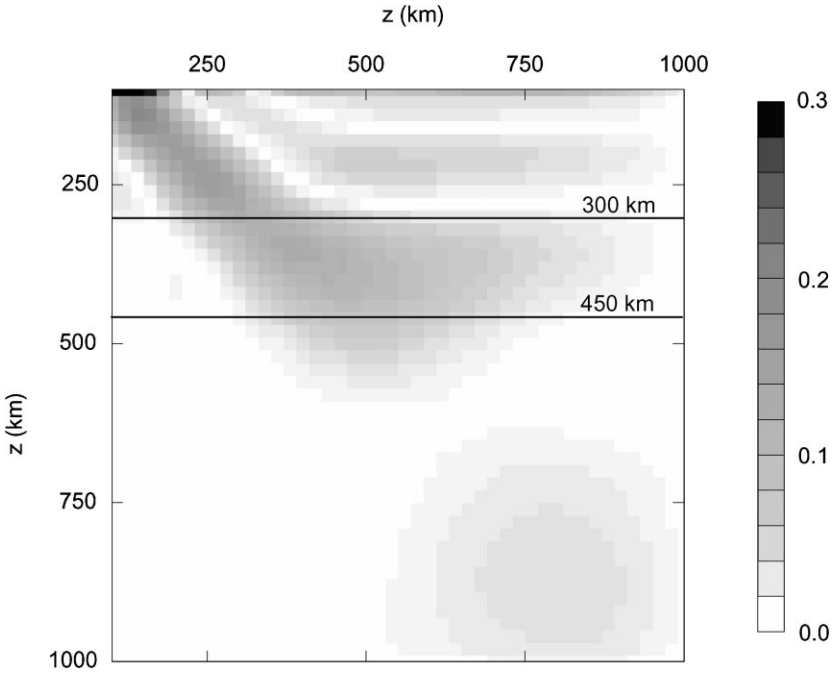


Fig. 7. Model resolution matrix for the preferred sub-continental scaling factor. Some smearing is present since $z = 300$ km depth (shallower horizontal line), and below $z = 450$ km the resolution is poor. In this example, original data are inverted for the sub-continental scaling factor in the window $\ell = 11$–16, and integration (7) is performed from $z = 1000$ km depth up to the surface. The damping factor is equal to 400. The viscosity model is MF2 and the element of surface is constant with $\mathrm{d}\varphi = 5^\circ$ on the equator.

of inversions with different values of the damping. For values of $\varepsilon$ smaller than those of our preferred model (and therefore, for rougher estimated model), $\zeta$ becomes negative at shallower depths (Fig. 8). Similarly, for higher values of $\varepsilon$ (not shown here), $\zeta$ changes sign deeper in the mantle. However, the shape of the function $\zeta(z)$ does not change dramatically. Rougher models result in slightly stronger radial variations in the layer 200–300 km, and significantly higher variances throughout the upper mantle. Variances are higher because a weaker damping allows bigger radial derivatives, and therefore wider ranges of values, for $\zeta$. Note that the preferred models (dashed curves in Fig. 8) remain within these error bars. In other words, weaker a priori information does not induce dramatic changes in the shape and amplitude of $\zeta$. Moreover, the difference between the sub-continental and sub-oceanic scaling factor is still present. Therefore, the damping factor is not a sensitive parameter. This result is important, since the determination of the best value of $\varepsilon$ is subjective.

### 4.3. Viscosity model

We made additional calculations to estimate the influence of the viscosity profile. The viscosity model does not appear explicitly in Eq. (3), but it is required to compute the geoid kernels $G_\ell(r)$. The model MF2 (Mitrovica and Forte, 1997) was built to provide a good fit of both the long-wavelength gravity anomalies and the relaxation times estimated from postglacial uplift. The first alternative model we have considered (FDW, Fig. 9a) has been constructed by Forte et al. (1993) to provide good fit of the degree 2 of the geoid. We have then used the model M2 of Peltier (1996) (PM2 in Fig. 9a). This model results from inversion of relative sea level variations induced by the postglacial uplift only. In PM2, the viscosity in the mid-lower mantle is about 10 times that in the mid-upper mantle. Finally, we have considered a model predicted by numerical experiments of thermal convection (cv2D, Fig. 9a). This model consists of two layers representing the upper and lower mantle. The reference

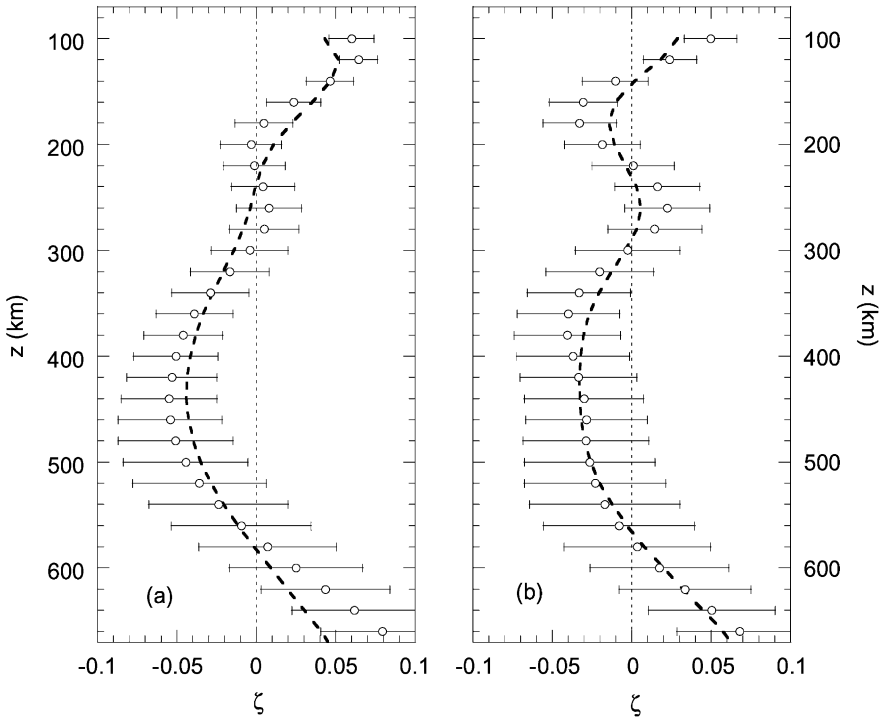


Fig. 8. Inverted scaling factor in the sub-continental (a) and sub-oceanic (b) upper mantle, for $\varepsilon = 200$ and $\varepsilon = 125$, respectively. The other parameters are the same as those in Fig. 4. The dotted curves represent the preferred sub-continental (a) and sub-oceanic (b) scaling factors.

viscosity of the lower layer is 10 times that of the upper layer, and the ratio of the top to the bottom viscosity of the upper and lower layer are $10^4$ and $10^3$, respectively. The viscosity is an exponential law of temperature, and temperature profiles are given by 2D-numerical experiments of convection (Deschamps and Sotin, 2000).

At depths shallower than 350–400 km, the scaling factors obtained for $\ell = 11$–16 and the viscosity models discussed above are very similar, for both sub-oceanic and sub-continental mantle (Fig. 9b and c). In particular, the depth at which the scaling factor becomes negative does not depend on the viscosity model. In each case, the sub-continental scaling factor has a local maximum around $z = 120$–140 km depth. In addition, if we consider the scaling factor obtained by inversion of the original $V_S$-anomalies, the variance reduction of the reconstructed to the observed gravity (or geoid) anomalies is nearly the same, whatever the viscosity model. At depths greater than 400 km, significant differences appear, depending on the viscosity model. To account for an eventual viscous layer at the top of the mantle, we modified the model MF2. Down to $z = 300$ km depth, we imposed $\mu/\mu_0 = 10^3$ (instead of $\mu/\mu_0 \sim 2$ in the original model) covering thus three orders of magnitude. Below 300 km, we let MF2 unchanged. However, inversions performed with this modified version of MF2 do not lead to significant differences in the model of scaling factor. Finally, we did an inversion in the (unlikely) case of a viscosity that decreases with depth (namely, the model symmetric to MF2 in respect with the $\log(\mu/\mu_0) = 0$ axis), and still found no significant differences down to $z = 400$ km depth. Thus, the nature of the scaling factor calculated in the uppermost mantle results from information in the data. Moreover, uncertainties on the radial model of viscosity do not broaden the variance in $\zeta$.

The geoid kernels for degrees higher than $\ell = 10$ peak in the uppermost mantle and have small values at depth greater than 1000 km. This feature is

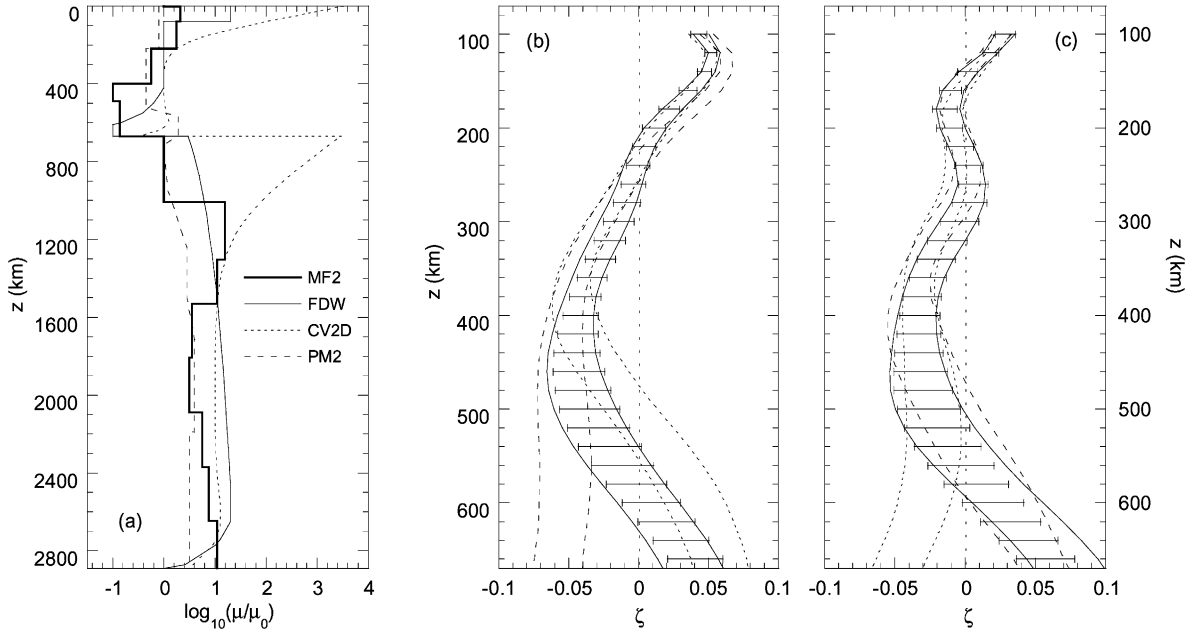


Fig. 9. Various possible viscosity profiles in the mantle (see text for references) (a); their corresponding inverted scaling factor in the sub-continental (b); and sub-oceanic (c) mantle. For each case, two curves are drawn, representing the minimal ($\bar{\zeta} - \sigma_\zeta$) and maximal ($\bar{\zeta} + \sigma_\zeta$) values of the scaling factor. Our preferred model (viscosity MF2) is indicated by the error bars. Data are filtered out for degrees $\ell = 11$–16, and Eq. (7) is integrated from $z = 1000$ km depth up to the surface. The damping factor is equal to 400 for continents, and 250 for oceans.

independent of the viscosity profile and may explain why, in the uppermost mantle, the model of scaling factor for $\ell = 11$–16 does not depend on this parameter. Indeed, by considering degrees $\ell = 2$–8 only we find that models of scaling factor for different viscosity profiles are slightly different even above $z = 400$ km. Some smaller differences are also present if one considers $\ell = 2$–16, but we do not observe dramatic changes in the shape and amplitude of $\zeta$.

Previous inversions of tomographic models and geodetic data have focused on the determination of a suitable viscosity model for the mantle (King and Masters, 1992; Forte et al., 1993, 1994b). Such studies have imposed a priori values of the scaling factor based on laboratory measurement. However the present results suggest that at depths smaller than 400 km, the scaling factor is not sensitive to realistic variations in the viscosity model. Therefore, in the uppermost mantle, it is more relevant to impose a viscosity profile and to invert for the scaling factor than to do the opposite.

### 4.4. Wavelength of the heterogeneities

In Eq. (3), we have assumed that the scaling factor does not depend on the spherical harmonic degree. To test this assumption, we did additional inversions for different windows of the spherical harmonics expansion, including degrees lower than $\ell = 11$ (Fig. 10). Calculations were made for the viscosity model MF2, and appropriate values of the damping factor. Because low-degree kernels have non-negligible values throughout the mantle, the integration (7) was performed from the core-mantle boundary up to the surface. Obviously, for $\ell = 11$–16, modification of the integral bounds does not change the results of the inversion at all. Down to $z = 350$ km depth, the models of scaling factor for $\ell = 2$–16 and $\ell = 11$–16 are similar. At greater depths, on the other hand, they differ significantly. The model of $\zeta$ for degrees $\ell = 2$–8 only is different from the others even in the uppermost mantle. Finally, by removing the lowest degrees ($\ell = 2$–4), the scaling factor is in good agreement

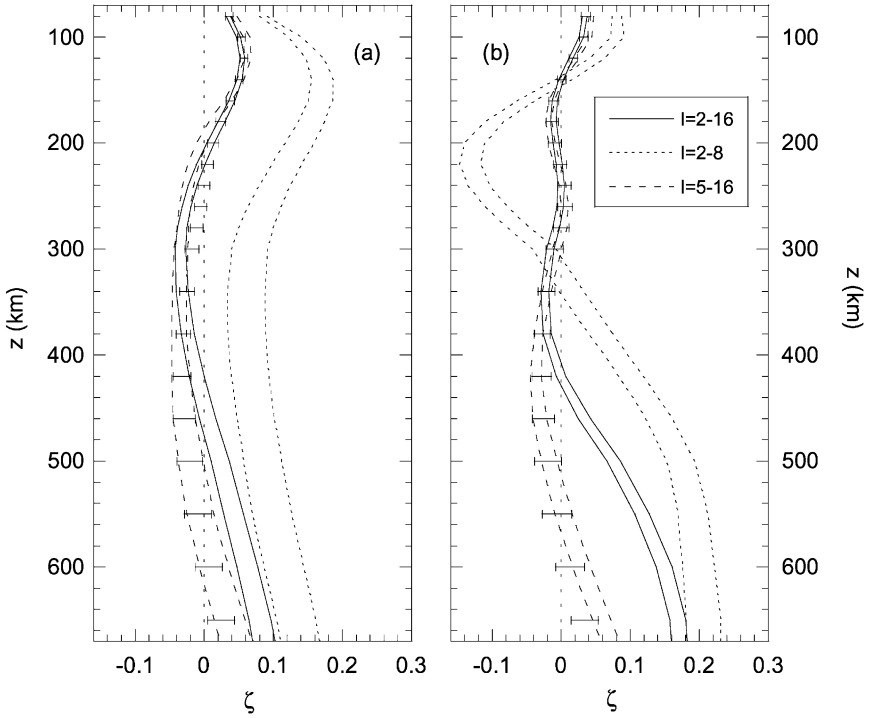


Fig. 10. Inverted scaling factor in the sub-continental (a) and sub-oceanic (b) mantle, for different windows of the data spectrum: $\ell = 2$–16, $\ell = 2$–8 and $\ell = 5$–16. For each case, two curves are drawn, representing the minimal $(\bar{\zeta} - \sigma_\zeta)$ and maximal $(\bar{\zeta} + \sigma_\zeta)$ values of the scaling factor. Our preferred model ($\ell = 11$–16) is indicated by the error bars. Eq. (7) is integrated from the core-mantle boundary up to the surface. For each calculation, the viscosity model is MF2. For continents (oceans) and $\ell = 2$–16, $\ell = 2$–8, $\ell = 5$–16 and $\ell = 11$–16, the damping factor is equal to 900, 450, 600 and 400 (500, 250, 450 and 250), respectively.

with the case $\ell = 11$–16 down to $z = 600$ km depth. In the deep mantle ($z \geq 350$ km), low degrees ($\ell = 2$–4) have therefore a strong influence on the scaling factor, but one can safely remove them to compute values of $\zeta$ in the uppermost mantle ($z \leq 350$ km).

A possible explanation is related to the shape of the geoid kernels and to the power spectrum of S16RLBM (Fig. 11). Down to $z = 300$ km depth, the low degrees ($\ell = 2$–4) do not dominate $V_S$-anomalies (Fig. 11a–c). In addition, the geoid kernels have small absolute values, compared to the higher degrees ($\ell = 8$–16) (Fig. 1b and c). For instance, in the layer $100 \leq z \leq 300$ km, $G_{\ell=2}$ increases from 0.1 to 0.05, whereas $G_{\ell=11}$ ranges between $-0.16$ and $-0.26$. At depths greater than 400 km, the dominant degree of $V_S$-anomalies is $\ell = 2$ (Fig. 11d and e). Moreover, at these depths, low degree geoid kernels have values comparable to or larger than those of the higher degrees. For low degrees, the absolute values of the quantity $K(r, \theta, \varphi)$ (Eq. (6)) at shallow depths are small, compared to those at depths greater than 400 km. As a result, the contribution of shallow depths to the gravity anomalies (Eq. (7)) is small, and $\zeta$ is not very well constrained. A similar effect happens for high degrees at depths greater than 350 km. The degree $\ell = 5$ dominates $V_S$-anomalies down to $z = 150$ km depth (Fig. 11a). However, the geoid kernel for $\ell = 5$ yields low values down to $z = 300$ km, and peaks around $z = 600$ km (Fig. 1b). For $\ell = 5$, the low geoid sensitivity balances the high $V_S$-signal, and the scaling factor for $\ell = 11$–16 is close to that for $\ell = 5$–16 (Fig. 10). This result emphasizes the robustness of the inversion.

The inversion is not very sensitive to parameters such as the viscosity profile and a priori information (smoothness in the present study). If one considers

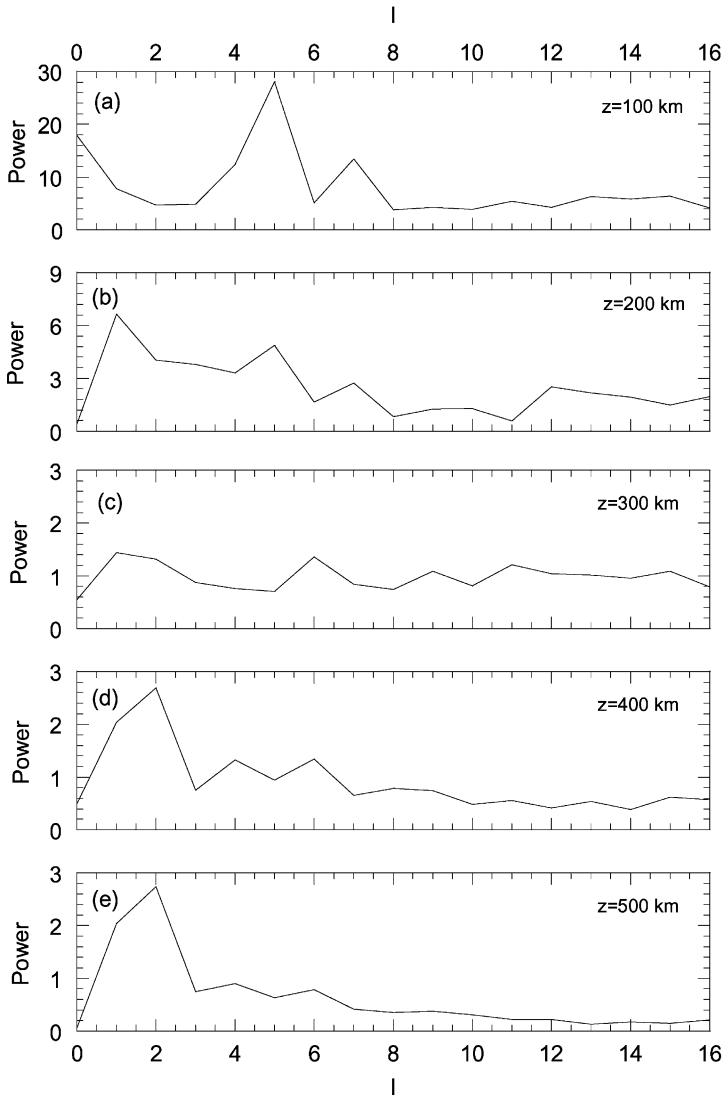


Fig. 11. Power spectrum of the global model S16RLBM at $z = 100$ km (a); $z = 200$ km (b); $z = 300$ km (c); $z = 400$ km (d); and $z = 500$ km (e). The dominant degrees are $\ell = 5$ down to $z = 150$ km, and $\ell = 2$ at depths greater than $z = 350$–400 km. In between these depths, the spectrum is flat.

different viscosity models and values of the damping factor, the shape and the amplitude of the function $\zeta(z)$ at depths shallower than 400 km does not change dramatically, and the continent–ocean difference is still present. Finally, we did calculations with the global S-wave model S20RTS (Ritsema et al., 1999), and found results very close to those obtained with S16RLBM in the uppermost mantle (small differences appeared in the amplitude of the scaling factor, but not in its shape). Therefore, we believe that the features reported in this section are quite robust.

## 5. Discussion

King and Masters (1992) assumed $\zeta = 0.4$ throughout the mantle, and inverted degrees $\ell = 2$–8 for the radial viscosity profile. By inverting S16RLBM and

EGM96 with their model MODLSHC, we have found a scaling factor and variance reduction similar to those obtained with the model MF2, for both $\ell = 2$–16 and $\ell = 11$–16. As shown in Section 4, in the uppermost mantle, inversions are more relevant for the scaling factor than for the radial viscosity model. Note that we do not account for lateral viscosity variations. Since in the uppermost mantle $\zeta$ does not depend strongly on the viscosity model, such lateral variations should only have limited consequences. The method used to compute geoid kernels (expansion of conservative equations in terms on generalized spherical harmonics) do not allow lateral variations of viscosity. However, an approximate and suitable way to account for lateral viscosity variations would be to consider regional studies with adapted viscosity models for each region.

Using gravity data up to $\ell = 12$, Kogan and McNutt (1993) performed joint inversions for Eurasia. They have tested different viscosity models depending on the region considered. Assuming a constant value for the scaling factor throughout the mantle, they found $\partial V_S/\partial\rho = 12$, or, using PREM as a reference model, $\zeta \sim 0.11$. For the sub-continental upper mantle, and using degrees $\ell = 2$–12 and the viscosity model MF2, the values of $\zeta$ predicted by the present method are close to but smaller than this value ($\zeta$ becomes negative at $z = 220$ km, and lies between 0.05 at $z = 80$ km and 0.1 at $z = 120$ km).

Forte et al. (1994b) performed joint inversions for the whole mantle, and proposed different models for the scaling factor, based on different possible parameterizations. In another study, Forte et al. (1994a) have inverted data separately for the scaling factors correlated ($\zeta_{co}$) and not correlated ($\zeta_{th}$) to the continent–ocean difference, using degrees $\ell = 2$–8 and a given model of viscosity. They assumed a general shape for the curve $\zeta(z)$ and found that in the upper mantle, $\zeta_{co}$ ranges between $-0.3$ and 0.3 and changes sign at $z \sim 300$ km depth. They interpreted this sign reversal as a signature of the stabilization of the continent–ocean heterogeneity. Once again, the values reported in the previous section are smaller, even for the case $\ell = 2$–16.

The major improvement of the present study is that it does not assume any a priori value or shape for the scaling factor. The model $\zeta(z)$ is determined only by the smoothed linear inversion of a tomographic model and gravity data, and thus it contains information brought by these data sets only.

Our preferred model is built with $\ell = 11$–16, which constitutes a second improvement. Low degree ($\ell = 2$–4) geoid kernels are mostly representative of the deep mantle, and they do not sample depths shallower than 350 km very well. On the contrary, geoid kernels for degrees higher than $\ell = 11$ do not sample the mantle below $z = 1000$ km depth, and have large absolute values in the shallow mantle. As pointed out in Section 4.4, this difference of sensitivity together with the power spectrum of S16RLBM result in significantly different values of the scaling factor below $z = 350$ km depth, whether one accounts for the low degrees or not. Degrees $\ell = 11$–16 are well-suited to study the uppermost mantle, and allow the resolution of the continent–ocean difference, which is present down to $z \sim 260$ km. However, by filtering $V_S$-anomalies between $\ell = 11$ and $\ell = 16$, one removes most of the seismic signal available at depths greater than $z = 400$ km (Fig. 11d and e). At depths, our preferred model is probably not relevant. To compute relevant values of the scaling factor in the transition zone and in the lower mantle, one must include low degrees. On the other hand, to detect compositional changes within the shallow sub-continental mantle one needs degrees higher than $\ell = 16$. This last task also requires regional tomographic models rather than a global model.

A final improvement is to perform inversions separately for the sub-continental and sub-oceanic mantle. This distinction is not equivalent to the inversions performed by Forte et al. (1994a). The differences between the sub-continental and sub-oceanic scaling factor can be used to interpret the continent–ocean difference. But in addition, separate models provide information about compositional changes within the sub-continental and sub-oceanic mantles: using Eq. (1), one can interpret the scaling factor models in terms of thermal and/or compositional lateral variations.

The difference in shape of the sub-oceanic and sub-continental scaling factors is related to the source of anti-correlation between gravity and $V_S$-anomalies, which is present below continents between 80 and 180 km. At these depths the sub-continental scaling factor is clearly positive, reaching a local maximum around $z = 120$ km. On the other hand, there is no significant correlation between gravity and $V_S$-anomalies

below oceans. Another important difference appears in the variance reduction of the reconstructed to the observed gravity anomalies. For $\ell = 11$–16, this variance reduction is significantly poorer for the sub-oceanic scaling factor (∼10%) than for the sub-continental scaling factor (∼30%). On the other hand, if one accounts for low degrees only ($\ell = 2$–8) the variance reduction to the observed gravity anomalies is higher for the sub-oceanic scaling factor (∼50%) than for the sub-continental scaling factor (∼30%). These observations suggest that intermediate-scale heterogeneities might play a more important role in the continental uppermost mantle than in the oceanic uppermost mantle. The oceanic regions seem to be well-explained by low degree anomalies only, and therefore may be dominated by large-scale structures, while the continental uppermost mantle may include more complexities, which are better accounted for by intermediate degrees anomalies.

A full interpretation of our results in term of chemical and/or thermal anomalies is beyond the scope of this paper. However, we now give some elements of comparison between available experimental data and the results of the present inversion.

Experimental values of $\zeta$ are usually deduced from the measurements of elastic properties of olivine (Isaac et al., 1989; Isaac, 1992), which is the dominant mineral of the mantle. Such values of $\zeta$ are based on the temperature derivative of $V_S$ and $\rho$, and therefore they account only for temperature variations. For olivine, the typical value of $\zeta$ at ambient pressure and $T = 1000$ K is equal to 0.45 (Isaac, 1992). Elastic properties of the other minerals of the upper mantle are less well documented. For a given mineralogical composition, numerical models can provide synthetic values of S-wave velocity and density based on the experimental values of the elastic and thermal parameters of each minerals (e.g. Davies and Dziewonski, 1975; Duffy and Anderson, 1989; Vacher et al., 1996). Following the model of Vacher et al. (1998), we have computed $V_S$-anomalies and density anomalies associated with pure temperature variations. The reference temperature and pressure are $T = 1280$°C and $p = 4$ GPa, respectively, and the mineralogical model is pyrolite (i.e. the volumic fraction of olivine is equal to 62%). The scaling factor resulting from these anomalies yields values around 0.37–0.38 (Fig. 12, dotted curve). The inverted values

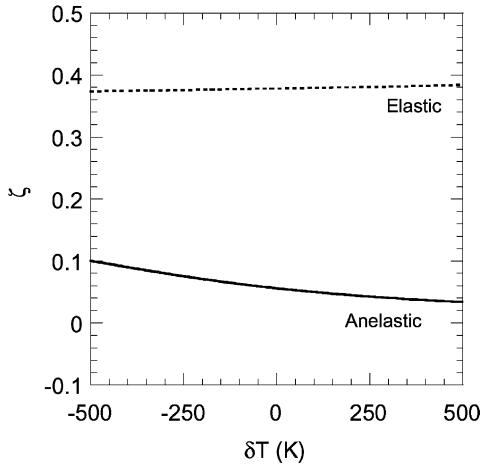


Fig. 12. Scaling factor for pure temperature variations ($\delta T$) predicted by experimental mineralogy. Anomalies of density and S-wave velocity are computed following the method of Vacher et al. (1998). The reference temperature is $T = 1280$°C, and the pressure is $p = 4$ GPa. The mineralogical model is pyrolite, as defined by Vacher et al. (1998). The dotted curve is based on laboratory measurement of elastic data performed at very high frequency. The plain curve accounts for anelasticity effects, using the model of quality factor Q1 of Goes et al. (2000) for a frequency $f = 0.1$ Hz.

of $\zeta$ reported in this study are significantly smaller, even if one considers only degrees $\ell = 2$–8 of the data. However, in the mantle, one must also account for chemical variations and possible additional effects such as anelasticity (see below). Moreover, elastic moduli depend on the pressure, and the scaling factor may also vary as a function of depth. Finally, extrapolation of laboratory measurements (elastic moduli and their temperature and pressure derivatives) to mantle pressures may induce additional errors.

In the Earth's mantle, anelasticity is responsible for attenuation of seismic waves (e.g. Anderson, 1989, pp. 279–302). Laboratory measurements of elastic data are usually performed at high frequencies (1 MHz and more). Such frequencies are much higher than the upper cut-off frequency of the absorption band. Therefore, laboratory measurements should be corrected before being used to compute velocities in the seismic band. Karato (1993) accounted for anelasticity to compute values of $\partial \ln V_S/\partial T$ and $\zeta$. To compute the anharmonic part of $\partial \ln V_S/\partial T$, he used the model of Duffy and Anderson (1989), which accounts for

pressure dependence of elastic parameters. He found that $\zeta$ increases from 0.2 to 0.3 in the upper mantle, and concluded that anelasticity damps the effects of thermal anomalies on seismic velocities. We have also introduced anelasticity effects in the model of Vacher et al. (1998) following the method proposed by Goes et al. (2000). For their model of quality factor Q1 and a frequency equal to 0.1 Hz, we obtained values of $\zeta$ around 0.05 (Fig. 12, plain curve). These values are in good agreement with our inverted values.

Unlike temperature variations, compositional changes do not have a well-defined influence on the scaling factor. For instance, the scaling factor can be either positive or negative, depending on the mineralogical variations considered. Using the method of Vacher et al. (1998), we have computed S-wave velocities and densities for mixes with two end-members (Olivine–Garnet and Olivine–Diopside). Increasing the volume fraction of diopside leads to higher densities and velocities, whereas increasing the volume fraction of garnet leads to higher densities, but smaller velocities. Therefore, the scaling factor is positive in the first case, and negative in the second one. Of course, the mineralogy of the mantle is much more complicated, and simultaneous variations in the volume fractions of different minerals could balance each others. Goes et al. (2000) have recently suggested that compositional variations may not induce strong $V_S$-anomalies. Therefore, chemical variations could explain partially, but maybe not completely, the differences in shape and amplitude between the model of Karato (1993), and that obtained by inversion of gravity and $V_S$-anomalies. Variations in the iron-content could also play a significant role. Since the model S16RLBM yields a good anti-correlation with the surface heat flux (Röhm et al., 2000), thermal processes in the uppermost mantle probably play an important role to explain the origin of the continental seismic lithosphere. Röhm et al. (2000) have proposed two possible thermal origins: (1) variations in the thickness of the thermal boundary layer; and (2) variations in the shallow radiogenic heat production. Positive values of the scaling factor, as those we observe above 200 km depth, are consistent with thermal origins. The decrease of the scaling factor with depth and its sign change could indicate that thermal (compositional) anomalies are progressively less (more) important, as depth is increasing. However, a systematic study is required to clear up the actual influence of temperature and compositional variations on the scaling factor.

## 6. Conclusions

The scaling factor relates relative density anomalies to relative $V_S$-anomalies and is therefore of great interest for the interpretation of seismological models. To invert for this scaling factor in the uppermost mantle, we have used spherical harmonic degrees $\ell = 11$–$16$ of gravity and S-wave velocity anomalies. This spatial window is well-adapted to the inference of intermediate size anomalies in the uppermost mantle. In the sub-continental mantle, the scaling factor has positive values down to $z \sim 220$ km depth. In the sub-oceanic mantle, the scaling factor is significantly different, and reaches zero-value at shallower depth. At depths greater than 260 km, the sub-continental and sub-oceanic models are close one to each other. These results are quite robust, but they hold in the uppermost mantle only, i.e. at depth shallower than 350 km. At greater depths, low degrees of the spherical harmonic expansion ($\ell = 2$–$4$) cannot be removed and the model of scaling factor depends on the radial model of viscosity. The observed differences between the sub-continental and sub-oceanic scaling factors suggest that intermediate-scale anomalies are more important below continents than below oceans. Finally, a rapid comparison between our results and experimental mineralogy yields significant discrepancies in the value of the scaling factor. Most of these discrepancies are explained if one accounts for anelasticity. The calculations presented in this paper may be refined to selected geographical areas using regional tomographic models. Regional models of the scaling factor would be a way to account for lateral viscosity variations and could be useful to explain the relative stability of major tectonic units, such as old cratons.

## Acknowledgements

John Woodhouse first pointed out the correlation between S16RLBM and gravity anomalies, which led us to carry out the present research. Gravity anomalies were computed using software developed at DEOS, Delft University of Technology. Roger

Haagmans and Arnoud de Bruijne kindly provided us this software and gave us some of their time for useful discussions about the geoid properties. Ernst Schrama and Nikolaos Pavlis provided us variances in EGM96 gravity anomalies. We thank two anonymous reviewers for constructing comments. This research was partly funded by The Netherlands Organization for Scientific Research (NWO, Grant 750.297.02).

## Appendix A. Generalized linear inversion

To solve Eq. (7), we used a generalized linear inversion, which minimize a linear combination of estimated errors and a priori information.

$$\boldsymbol{m}^{\mathrm{est}} = \boldsymbol{G}^{-\mathrm{g}}\boldsymbol{d} \tag{A.1}$$

where $\boldsymbol{d}$ is the data vector (here, the gravity anomalies), $\boldsymbol{m}^{\mathrm{est}}$ the estimated model (the scaling factor in our problem), and $\boldsymbol{G}^{-\mathrm{g}}$ the generalized inverse matrix.

$$\boldsymbol{G}^{-\mathrm{g}} = [\boldsymbol{G}^{\mathrm{T}}\boldsymbol{G} + \varepsilon^2\boldsymbol{W}]^{-1}\boldsymbol{G}^{\mathrm{T}} \tag{A.2}$$

where the superscript T denotes the transpose matrix. The matrix $\boldsymbol{G}$ is the kernel matrix. In our example (Eq. (7)), it contains the product $K$ of the relative S-wave velocity anomalies with the geoid kernels (Eq. (6)). The matrix $\boldsymbol{W}$ contains a priori information, and it is weighted by the damping factor $\varepsilon$. Here, we impose our model to vary smoothly as a function of depth. Therefore, $\boldsymbol{W}$ is defined by the product of the flatness matrix $\boldsymbol{F}$ with its transpose.

$$\boldsymbol{W} = FF^{\mathrm{T}}, \quad \text{where}$$
$$\boldsymbol{F} = \begin{pmatrix} -1 & 1 & & & & \\ & -1 & 1 & & & \\ & & \cdots & \cdots & & \\ & & & \cdots & \cdots & \\ & & & & -1 & 1 \end{pmatrix} \tag{A.3}$$

Note that the dimension of $\boldsymbol{F}$ is $M \times (M+1)$, where $M$ is the dimension of the model. To invert the matrix in the brackets in Eq. (A.2), we have used a LU decomposition method.

The resolution matrix $\boldsymbol{R}$ provides information about the resolution of the model.

$$\boldsymbol{R} = \boldsymbol{G}^{-\mathrm{g}}\boldsymbol{G} \tag{A.4}$$

If the estimated model is perfectly resolved, $\boldsymbol{R}$ is equal to the identity matrix. To estimate the quality of the model, one might also consider its norm $L$, its roughness $S$ (that is to say the norm of the model derivative), and the variance reduction of the reconstructed data to the observed data ($X$).

$$L = (\boldsymbol{m}^{\mathrm{est}^{\mathrm{T}}}\boldsymbol{m}^{\mathrm{est}})^{1/2} \tag{A.5}$$

$$S = (\boldsymbol{m}^{\mathrm{est}^{\mathrm{T}}}W m^{\mathrm{est}})^{1/2} \tag{A.6}$$

$$X = 1 - \frac{\sum_{i=1}^{N}(d_i - d_i^{\mathrm{est}})^2}{\sum_{i=1}^{N} d_i^2} \tag{A.7}$$

where $N$ is the dimension of the data vector, and $\boldsymbol{d}^{\mathrm{est}} = Gm^{\mathrm{est}}$ the reconstructed data vector. $S$ and $X$ decrease as the damping factor ($\varepsilon$) increases. Usually, one defines the preferred model as being the best compromise between the data information and a priori information (here the roughness). The damping factor $\varepsilon$ is therefore chosen on the trade-off curve, which plot the misfit ($1 - X$) as a function of the roughness (e.g. Fig. 5).

To account for the uncertainties of the elements of $\boldsymbol{G}$, we added random simulated errors to these elements, and performed an inversion with each perturbed matrix. This lead to a collection of $Z$ perturbed models ($\boldsymbol{m}^{\mathrm{per}}$). The mean model over this collection ($\bar{\boldsymbol{m}}$) and its variance ($\boldsymbol{\sigma_m}$) are given by

$$\bar{\boldsymbol{m}} = \frac{1}{Z}\sum_{j=1}^{Z}\boldsymbol{m}_j^{\mathrm{per}} \tag{A.8}$$

$$\boldsymbol{\sigma}_{\boldsymbol{m}}^2 = \frac{1}{Z}\sum_{j=1}^{Z}(\boldsymbol{m}_j^{\mathrm{per}} - \bar{\boldsymbol{m}})^2 \tag{A.9}$$

The length ($\bar{L}$), the smoothness ($\bar{S}$) and the variance reduction ($\bar{X}$) of the mean model are given by Eqs. (A.5)–(A.7), where $\boldsymbol{m}^{\mathrm{est}}$ must be replaced by $\bar{\boldsymbol{m}}$. To be relevant, the mean model and its variance must be computed with a large enough collection of perturbed models. To test this condition, one can plot $\bar{L}$ and $\bar{S}$ as a function of $Z$. The model $\bar{\boldsymbol{m}}$ is statistically relevant when $\bar{L}$ and $\bar{S}$ oscillate around stationary values (Fig. 3).

## References


Anderson, D.L., 1989. Theory of the Earth, Blackwell, Boston.

Davies, G.F., Dziewonski, A.M., 1975. Homogeneity and constitution of the Earth's lower mantle and outer core. Phys. Earth Planet. Inter. 10, 336–343.

Deschamps, F., Sotin, C., 2000. Inversion of 2D numerical convection experiments for a strongly temperature-dependent viscosity fluid. Geophys. J. Int. 143, 204–218.

Duffy, T.S., Anderson, D.L., 1989. Seismic wave speeds in mantle minerals and the mineralogy of the upper mantle. J. Geophys. Res. 94, 1895–1912.

Dziewonski, A.M., Anderson, D.L., 1981. Preliminary reference Earth model. Phys. Earth Planet. Inter. 25, 297–356.

Forte, A.M., Peltier, W.R., 1987. Plate tectonics and aspherical Earth's structure: the importance of poloidal–toroidal coupling. J. Geophys. Res. 92, 3645–3679.

Forte, A.M., Peltier, W.R., 1991. Viscous flow models of global geophysical observables. 1. Forward problems. J. Geophys. Res. 96, 20131–20159.

Forte, A.M., Dziewonski, A.M., Woodward, R.L., 1993. Aspherical structure of the mantle, tectonic plate motions, non-hydrostatic geoid, and topography of the core-mantle boundary. In: LeMouël, J.-L., Smylie, D.E., Herring, T., Dynamics of the Earth's Deep Interior and Earth Rotation, Vol. 72. Geophysics Monographic Series, Washington, DC, pp. 135–166.

Forte, A.M., Dziewonski, A.M., O'Connell, R.J., 1994a. Thermal and chemical heterogeneity in the mantle: a seismic and geodynamic study of continental roots. Phys. Earth Planet. Inter. 92, 45–55.

Forte, A.M., Woodward, R.L., Dziewonski, A.M., 1994b. Joint inversions of seismic and geodynamic data for models of three-dimensional mantle heterogeneity. J. Geophys. Res. 99, 21857–21877.

Goes, S., Govers, R., Vacher, P., 2000. Shallow mantle temperatures under Europe from P and S wave tomography. J. Geophys. Res. 105, 11153–11169.

Haagmans, R., de Bruijne, A., de Min, E., 1998. A procedure for combining gravimetric geoid models and independent geoid data, with an example in the north sea region. DEOS Progress Letters, 98.1, Delft University Press, http://www.geo.tudelft.nl/fmr/deosletter.

Isaac, D.G., 1992. High-temperature elasticity of iron-bearing olivines. J. Geophys. Res. 97, 1871–1885.

Isaac, D.G., Anderson, O.L., Goto, T., Suzuki, I., 1989. Elasticity of single-crystal forsterite measured to 1700 K. J. Geophys. Res. 94, 5895–5906.

Jordan, T.H., 1975. The continental tectosphere. Rev. Geophys. Space Phys. 13, 1–12.

Karato, S.I., 1993. Importance of anelasticity in the interpretation of seismic tomography. Geophys. Res. Lett. 20, 1623–1626.

King, S.D., Masters, G., 1992. An inversion for radial viscosity structure using seismic tomography. Geophys. Res. Lett. 19, 1551–1554.

Kogan, M.K., McNutt, M.K., 1993. Gravity field over northern Eurasia and variations in the strength of the upper mantle. Science 259, 473–479.

Lemoine, F.G., Kenyon, S.C., Factor, J.K., Trimmer, R.G., Pavlis, N.K., Chinn, D.S., Cox, C.M., Klosko, S.M., Luthcke, S.B., Torrence, M.H., Wang, Y.M., Williamson, R.G., Pavlis, E.C., Rapp, R.H., Olson, T.R., 1998. The development of the joint NASA GSFC and National Imagery Mapping Agency (NIMA). Geopotential Model EGM96, NASA/TP-1998-206861, NASA, GSFC, Greenbelt, MD 20771.

Li, X.-D., Romanowicz, B., 1996. Global mantle shear velocity model developed using nonlinear asymptotic coupling theory. J. Geophys. Res. 101, 22245–22272.

Mitrovica, J.X., Forte, A.M., 1997. Radial profile of mantle viscosity: results from the joint inversion of convection and postglacial rebound observables. J. Geophys. Res. 102, 2751–2769.

Nakiboglu, S.M., 1982. Hydrostatic theory of the Earth and its mechanical implications. Phys. Earth Planet. Inter. 28, 302–311.

Nataf, H.-C., Ricard, Y., 1996. 3SMAC: an a priori tomographic model for upper mantle based on geophysical modeling. Phys. Earth Planet. Inter. 95, 101–122.

Peltier, W.R., 1996. Mantle viscosity and ice-age ice sheet topography. Science 273, 1359–1364.

Press, W.H., Flannery, B.P., Teukolsky, S.A., Vetterling, W.T., 1989. Numerical Recipes. Cambridge University Press, Cambridge, 702 pp.

Ritsema, J., van Heijst, H.J., Woodhouse, J.H., 1999. Complex shear velocity structure imaged beneath Africa and Iceland. Science 286, 1925–1928.

Röhm, A., Snieder, R.K., Goes, S., Trampert, J., 2000. Thermal structure of continental upper mantle inferred from S-wave velocity and surface heat flow. Earth Planet. Sci. Lett. 181, 395–407.

Snieder, R.K., Trampert, J., 1999. Inverse problems in geophysics. In: Wirgin, A. (Ed.), Wavefield Inversion. Springer, New York, pp. 119–190, http://samizdat.mines.edu.

Su, W.J., Dziewonski, A.M., 1997. Simultaneous inversions for 3-D variations in shear and bulk velocity in the mantle. Phys. Earth Planet. Inter. 100, 135–156.

Trampert, J., Woodhouse, J.H., 1995. Global phase velocity maps of Love and Rayleigh waves between 40 and 150 s. Geophys. J. Int. 122, 675–690.

Vacher, P., Mocquet, A., Sotin, C., 1996. Comparison between tomographic structures and models of convection in the upper mantle. Geophys. J. Int. 124, 45–56.

Vacher, P., Mocquet, A., Sotin, C., 1998. Computation of seismic profiles from mineral physics: the importance of non-olivine components for explaining the 660 km depth discontinuity. Phys. Earth Planet. Inter. 106, 275–298.

Woodhouse, J.H., Trampert, J., 1995. Global upper mantle structure inferred from surface wave and body wave data. EOS Trans. AGU F422.